

CAPE: A CLIP-Aware Pointing Ensemble of Complementary Heatmap Cues for Embodied Reference Understanding

Fevziye Irem Eyiokur¹

Dogucan Yaman¹

Hazım Kemal Ekenel²

Alexander Waibel^{1,3}

¹Karlsruhe Institute of Technology, ²Istanbul Technical University, ³Carnegie Mellon University

irem.eyiokur@kit.edu

Abstract

We address the problem of Embodied Reference Understanding, which involves predicting the object that a person in the scene is referring to through both pointing gesture and language. Accurately identifying the referent requires multimodal understanding: integrating textual instructions, visual pointing, and scene context. However, existing methods often struggle to effectively leverage visual clues for disambiguation. We also observe that, while the referent is often aligned with the head-to-fingertip line, it occasionally aligns more closely with the wrist-to-fingertip line. Therefore, relying on a single line assumption can be overly simplistic and may lead to suboptimal performance. To address this, we propose a dual-model framework, where one model learns from the head-to-fingertip direction and the other from the wrist-to-fingertip direction. We further introduce a Gaussian ray heatmap representation of these lines and use them as input to provide a strong supervisory signal that encourages the model to better attend to pointing cues. To combine the strengths of both models, we present the CLIP-Aware Pointing Ensemble module, which performs a hybrid ensemble based on CLIP features. Additionally, we propose an object center prediction head as an auxiliary task to further enhance referent localization. We validate our approach through extensive experiments and analysis on the benchmark YouRefIt dataset, achieving an improvement of approximately 4 mAP at the 0.25 IoU threshold.

1. Introduction

Embodied Reference Understanding (ERU) [11] is the task of identifying a specific object in a visual scene based on language instructions and pointing cues in the image. It plays a key role in real-world applications like human-robot interaction, assistive robotics, and augmented reality, where systems must understand which object a person refers to.

While grounding models [37] have made significant

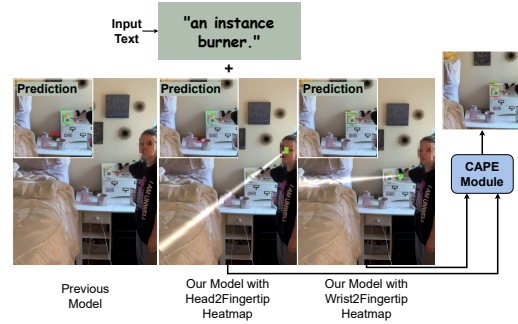


Figure 1. Example where a previous model fails. Our model M_{H2F} also fails due to distractions from other objects along the head-to-fingertip pointing line. However, our model M_{W2F} correctly detects the object, and CAPE selects this as the final prediction. This shows the flexibility and robustness of our approach.

progress in detecting objects mentioned in natural language, they often fall short in ERU task, particularly in ambiguous scenes. When multiple instances of the same object type are present, these models tend to detect all matching candidates without the ability to disambiguate and identify the specific target intended by the user. Moreover, when the textual instruction itself is vague or ambiguous, grounding models struggle even further, often failing to identify the correct target object or producing no confident prediction at all due to the inherent ambiguity. This limitation highlights the need for additional disambiguation cues, embodied gesture signals, that can help resolve referential ambiguity and enable accurate identification of the intended object. Therefore, both embodied gesture signals and language reference are crucial to identify the referent. In ERU, two main challenges arise. (1) identifying candidate objects from the text, as in standard grounding tasks, and (2) interpreting the pointing cue from visual input to guide the final prediction. The latter requires understanding human pose, inferring pointing direction, and handling visual complexities like perspective, occlusion, and depth.

In [11], first time ERU task is defined and a multimodal YouRefIt dataset is proposed. They also proposed a method that combines textual and visual inputs along with PAF [7] and predicted saliency maps [33] to help localize the human and narrow down the potential referent. While these inputs lead to improved performance, the model still exhibits suboptimal accuracy in many cases, particularly due to its inability to properly follow the pointing instructions. Building on this, the Touch-Line Transformer [35] introduces a novel approach by predicting a Virtual Touch-Line and applying losses that encourage the model to focus on the head-to-fingertip direction, which they find often aligns closely with the intended referent [24, 44]. Although this method achieves significant gains, it still faces challenges. The model occasionally overlooks the pointing line, as it is not explicitly provided as input. Instead, it predicts head, fingertips, and arm position to encourage attention in that direction. More importantly, the head-to-fingertip direction does not always align with the target. In some scenarios, the accurate pointing direction follows a line from the hand alone (e.g., wrist-to-fingertip), rather than from the head (Fig. 1). These observations suggest that while head-to-fingertip direction offers valuable guidance, it is not sufficient on its own to fully resolve the complexity of the task.

To tackle these challenges, we propose a dual-model framework that leverages complementary pointing cues. Both models take as input a referring expression and an image with a pointing gesture, along with an additional heatmap that encodes the pointing direction. One model utilizes a head-to-fingertip heatmap, while the other uses a wrist-to-fingertip heatmap, capturing different aspects of the pointing behavior. Their predictions are integrated via a CLIP-Aware Pointing Ensemble (CAPE) module, which effectively combines the strengths of both models. Additionally, we introduce an auxiliary objective to predict the object center, providing an extra supervisory signal that further enhances grounding accuracy. Our contributions are: (1) We propose using heatmap as extra modality to guide our end-to-end reference object detection model to focus on pointing information more. (2) We propose two parallel complementary models to focus on head-to-fingertip and wrist-to-fingertip pointing lines, to individually alleviate inherent challenges of the task. (3) We present CAPE module to effectively ensemble two complementary models. (4) We introduce object center prediction head to enhance prediction accuracy by focusing on finding the object without considering the precise bounding box.

2. Related Work

Referring Expression Comprehension (REC) In REC [23, 31, 42, 46, 47, 72], the goal is to identify a specific region in an image based on a given referring expression. In contrast to traditional object detection, REC

interprets free-form text and can locate objects from any category, including previously unseen ones. Similarly, OV-DETR [73] integrates image and text embeddings from a CLIP model as queries within the DETR [9] to generate category-specific bounding boxes. ViLD [19] distills knowledge from a CLIP teacher model into an R-CNN-like detector [18], enabling region embeddings to capture semantic information from language. GLIP [17] formulates object detection as a grounding task, using additional grounding datasets to align visual regions with textual phrases. DetCLIP [71] enriches its knowledge base using generated pseudo labels. While YOLO-World [12] extends traditional YOLO object detection [50] to an open-world setting, GroundingDINO [37] aligns visual and textual features to detect arbitrary objects described by free-form text. Recently, LMMs [1, 3, 5] get attention for their superior performance in visual grounding [10].

Nonverbal Communication for Referent Some studies [6, 20, 21, 25, 29, 45, 51, 53, 55–64, 66–68] use gaze target detection as a nonverbal cue, however, gaze alone is unreliable due to distractions and the absence of a clear pointing moment. It is typically localized frame by frame and often used to support conversation [4, 8]. In [43], a multimodal exophora resolution method is proposed to disambiguate demonstrative expressions like “that one” by integrating object categories, pointing gestures, and prior environmental knowledge. [14] introduced an interactive robot dialogue system that uses multimodal interaction and pointing line estimation to accurately identify referent with an iterative correction process. Their follow-up work [15] extended this by recognizing unseen objects using a Region Proposal Network and VL-T5 multimodal network [13], moving beyond general object classes from benchmarks like MSCOCO [36] to attribute-based object recognition. On the other hand, several datasets have been collected to incorporate nonverbal cues, but most remain in simulated domains due to accessibility and controllability [2, 26–28].

Embodied Reference Understanding (ERU) ERU is a recent advancement of REC that considers the subject’s position while pointing at a reference object. Chen et al. [11] introduced the task and benchmarks using both verbal (text) and nonverbal (pointing gesture) cues. Their model leverages predicted saliency maps and PAF [7] as gestural features to better perceive pointing direction and detect referents. To address ambiguities caused by camera perspective, [52] mapped scenes to 3D coordinates using depth estimation and subject position for spatial attention, but this only yielded modest improvements. Li et al. [35] further improved ERU using an MDETR-based [30] model, introducing a “virtual-touch-line” from eye to fingertip and predicting its vector alongside bounding boxes. In this work,

we also use a transformer-based multimodal object detector similar to MDETR [30]. However, instead of predicting a single line vector, we extend the visual-touch-line concept to a pointing heatmap representing the focus of attention. To capture different pointing variations, we use two different heatmaps processed in parallel networks. Some recent works [39, 40] have extended ERU task to 3D embodied settings. ScanERU [39] introduced the first 3D-ERU benchmark by inserting human avatars into existing 3D datasets, but relied on manual placement. In contrast, Ges3ViG [40] improves realism and scalability by automating avatar insertion, generating gesture-aware instructions, and incorporating human localization into the grounding pipeline.

3. Methodology

Problem Definition In ERU, given an RGB image $x_{img} \in \mathbb{R}^{3 \times H \times W}$ and a text input $x_{text} \in \mathbb{N}^L$, we predict a bounding box $x_{bbox} \in \mathbb{R}^4$ corresponding to an object referenced by the text and indicated by a pointing gesture in the image. We propose using an additional pointing heatmap $x_{phm} \in \mathbb{R}^{1 \times H \times W}$ to supervise the model better focus on the visual pointing reference.

3.1. Model Architecture

Fig. 2 illustrates our architecture, which consists of a large-scale text encoder, image encoder, and heatmap encoder. The outputs of these encoders are concatenated and fed into a transformer [65] encoder block. Subsequently, a transformer decoder processes the encoder output to generate predictions through task-specific heads. In this work, we introduce two networks that share the same architecture but are trained independently. The first network (M_{W2F}) receives a heatmap generated from the wrist-to-fingertip line, while the second (M_{H2F}) uses a heatmap derived from the head-to-fingertip line. Finally, a CLIP-Aware Pointing Ensemble (CAPE) module combines the outputs of these two complementary models to enhance overall performance.

Encoders We use a pretrained ROBERTA [38] which is a robustly optimized version of BERT [16] as the text encoder to obtain textual embeddings from the input text. To obtain image embeddings, $F_I \in \mathbb{R}^{2048 \times 8 \times 8}$, we utilize a pretrained ResNet-101 [22]. Since the pointing heatmap (x_{phm}) is a sparse representation, we choose a lightweight encoder, ResNet-18 [22], to embed it: $F_{phm} \in \mathbb{R}^{256 \times 8 \times 8}$. This choice not only improves the computational efficiency of the network but also helps prevent redundant information in the final concatenated feature representation, which could otherwise harm the model’s learning capacity.

Transformer encoder After obtaining the embeddings from three encoders, we first apply a 1×1 convolution

to each embedding individually to project their channel dimensions to 256. Next, we flatten the spatial dimensions of the embedding into a single dimension, converting them into sequences of tokens. For example, for the heatmap embedding: $F_{phm}^S = \text{flatten}(\text{Conv}_{1 \times 1}(F_{phm})) \in \mathbb{R}^{64 \times 256}$. We then concatenate the three embeddings at the sequence level to form the final representation, which is fed into the transformer encoder. It processes this concatenated input to learn multimodal representations.

Transformer decoder We feed the multimodal representation output from the transformer encoder into the transformer decoder. Additionally, we provide a set of learnable object queries and gestural keypoint queries. The transformer decoder is responsible for generating object output embeddings and gestural output embeddings.

Prediction head The object and gestural output embeddings produced by the transformer decoder serve as inputs to our prediction heads. These heads are responsible for predicting candidate bounding boxes for the referent, gestural keypoints (pointing direction prediction head in Fig. 2), which predicts eye, fingertip, wrist coordinates as well as arm class, and center points of the referent. Finally, we select one bounding box prediction, one center point and a pair of gestural keypoints with the highest confidence scores as the final prediction. Please note that we use multi-layer perceptrons (MLPs) as the prediction heads.

3.2. Pointing Heatmap Modality Learning

Incorporating a heatmap that represents the pointing direction provides a valuable spatial priors for the network, especially considering the fact that the existing models in this field tend to give less attention to the visual pointing. This explicit encoding pointing direction helps localize the target region by guiding the model’s attention toward direction and areas that are more likely to be referenced. This is particularly beneficial in real-world, cluttered scenes where gesture interpretation is inherently ambiguous.

How should we create heatmap? The VTL [35] demonstrates superior performance in most cases, as it effectively captures the intended pointing direction by leveraging both the fingertip position and the head orientation. Human pointing gestures are typically guided by visual attention: we often align our finger with the target object based on our eye-level perspective [35]. Consequently, the head-to-fingertip line serves as a strong proxy for the true pointing intent, integrating both gaze and gesture cues. However, the VTL is not universally reliable. In certain scenarios, the performer may be looking elsewhere (for instance, toward a robot or camera) rather than at the intended object. Additionally, in cases involving extreme viewing angles or

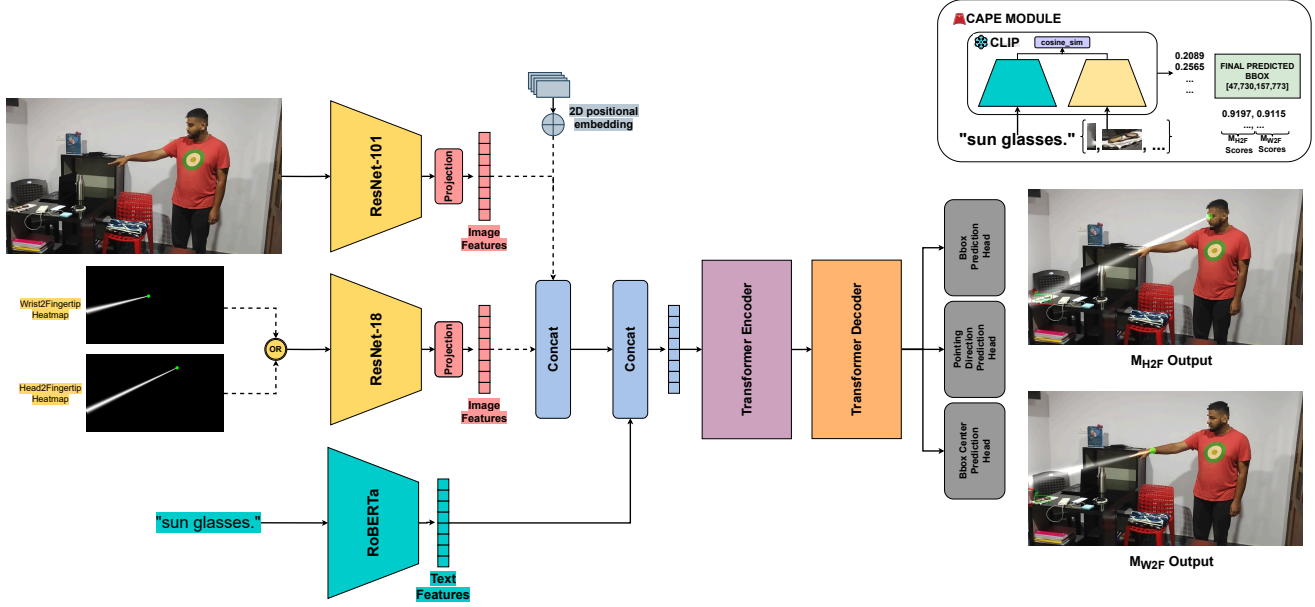


Figure 2. Overall network architecture. M_{H2F} and M_{W2F} share the same architectural design, therefore, only one model is illustrated. The two different heatmaps are shown for visualization purposes: M_{H2F} uses a head-to-fingertip heatmap, while M_{W2F} uses a wrist-to-fingertip heatmap.

occluded head poses, the head orientation may become ambiguous or misleading. In such situations, the local orientation of the hand, as approximated by the wrist-to-fingertip line, can offer complementary directional cues that help disambiguate the pointing gesture. We hypothesize that heatmaps derived from the head-to-fingertip and wrist-to-fingertip lines provide complementary information. Therefore, we generate heatmaps that incorporate both information. For the head-to-fingertip heatmap (x_{phm}^{H2F}), we use the eye coordinates as the starting point and draw a line toward the edge of the image, passing through the fingertip. Similarly, for the wrist-to-fingertip heatmap (x_{phm}^{W2F}), we start from the wrist and draw a line to the edge of the image through the fingertip point. To generate these heatmaps, we apply a Gaussian Ray Heatmap (See Appendix B).

How should we integrate these heatmaps? The next important question is how to integrate these heatmaps effectively. We explore two different approaches. In the first approach, we merge the two heatmaps ($x_{phm}^{H2F} + x_{phm}^{W2F}$) and feed the combined input into a single network to examine whether the model can implicitly learn to utilize both sources of information and determine the most appropriate direction based on the human pose. In the second approach, we train two identical networks independently and ensemble them: one using the head-to-finger heatmap (M_{H2F}) and the other using the wrist-to-fingertip heatmap (M_{W2F}). We empirically find that the second approach yields better performance. As expected, it allows us to train two com-

plementary networks. Notably, the network trained with the head-to-fingertip heatmap (M_{H2F}) demonstrates significant improvements. In contrast, the first approach results in only subtle enhancement, and the model fails to effectively leverage both sources of information to determine the pointing direction (see Tab. 3 Setup G). Its behavior closely resembles the head-to-fingertip-only scenario. However, due to the presence of additional wrist-to-fingertip line in the merged heatmap, the model experiences contradictory information, ultimately leading to reduced accuracy than head-to-fingertip heatmap-only setup.

Where should we inject these heatmaps? We empirically find that the most effective way to leverage heatmaps is to use a separate encoder to extract heatmap embeddings, which are then concatenated with the output of the image encoder. It enables us to preserve the pretrained image encoder and allows the dedicated heatmap encoder to extract rich, modality-specific information.

3.3. CLIP-Aware Pointing Ensemble (CAPE)

We introduce an inference time ensemble module to increase the performance by benefiting from two complementary models, M_{H2F} and M_{W2F} . CAPE is an adaptive scoring method that combines model confidence and CLIP-based similarity in a size-aware manner effectively. (1) For each prediction (top-2 predictions from both models), we compute a normalized CLIP score [48]. We sum pointing models' confidence scores with the CLIP scores to obtain

the fused score (CLIP Fusion in Tab. 5). (2) We calculate CLIP scores for the top-1 predictions of both models. If the confidence scores of the second-highest predictions exceed a threshold, we also compute their CLIP scores. Finally, we select the prediction with the highest CLIP score from among these candidate boxes (CLIP-Only Top-2 + Threshold=0.95 in Tab. 5). CAPE applies strategy (1) when the referent is a small object (defined as occupying less than 0.48% of the image area, following [11]) to avoid relying solely on the CLIP prediction, as CLIP becomes less reliable for smaller objects. For all other objects, strategy (2) is used (see Appendix C.5 for details). This hybrid approach leverages the strengths of both signals while adapting to object scale. All thresholds and selection rules were tuned on the validation set to avoid test-time overfitting.

3.4. Gestural Signal Learning

Referent alignment loss Following [35], we incorporate a referent alignment loss (L_{RA}) to enforce consistency between the predicted referent and the VTL. The core idea is that a correct referent should be geometrically aligned with the pointing direction. To quantify this alignment, we compute the cosine similarity between the eye-to-fingertip vector and the eye-to-object vector, defined as:

$$CS_p = \cos_sim((x_f - x_e, y_f - y_e), (x_o - x_e, y_o - y_e)) \quad (1)$$

where (x_e, y_e) and (x_f, y_f) are the eye and the fingertip coordinates. (x_o, y_o) are the center of the predicted bounding box. We compute the same similarity using GT bounding box to obtain CS_{GT} . The referent alignment loss then penalizes deviations between the predicted and GT alignment:

$$L_{RA} = ReLU(CS_p - CS_{GT}) \quad (2)$$

Please note that for both CS_p and CS_{GT} , we use GT eye and fingertip coordinates to ensure accurate directional representation. We apply this loss during the training of the model M_{H2F} , which uses the head-to-fingertip heatmap as reference. For training the M_{W2F} model, which utilizes the wrist-to-fingertip heatmap, we replace the eye coordinates with wrist coordinates. The rest remains unchanged, as we similarly aim to maximize the directional correlation.

Object center prediction In our task, identifying the correct referent and accurately localizing it are two distinct but equally important challenges. To enhance the localization capability of the model, we decouple the prediction of the object center from the rest of the bounding box regression. Specifically, we introduce an additional prediction head implemented as a MLP at the end of the network. This head is dedicated to predicting the (x, y) coordinates of the referent object’s center, independently from the standard bounding

box regression head. During training, we supervise this center prediction using the L1 loss between the predicted and GT center coordinates:

$$L_{center} = ||(x_o^{GT}, y_o^{GT}) - (x_o^p, y_o^p)||_1 \quad (3)$$

This explicit supervision encourages the model to focus on spatial alignment and leads to more accurate object localization, especially in scenes with dense or overlapping objects. Moreover, this center prediction serves as an auxiliary task, which improves the representational capacity of the model by encouraging the visual backbone to learn richer geometric and spatial features. We apply this auxiliary head and its corresponding loss to both models. Since this head is used only during training, it introduces no additional computational overhead during inference.

Gesture prediction In addition to the bounding box and object center predictions, our model incorporates several auxiliary heads to predict task-specific features, including eye (wrist in M_{W2F}) and fingertip coordinates, and arm classification (See prediction head in Sec. 3.1). For each prediction, we apply a standard L1 loss between the predicted and GT data, which encourages spatial attention to task-relevant regions such as the eyes and fingertips, enhancing the model’s understanding of referential gestures. Moreover, we apply cross-entropy loss to classify whether the predicted gestural keypoints are correct.

Total loss We define our objective as follows:

$$L = \lambda_1 L_b + \lambda_2 L_{RA} + \lambda_3 L_{center} + \lambda_4 L_g + \lambda_5 L_t + \lambda_6 L_c \quad (4)$$

where L_b is bounding box loss and it is the combination of L1 and GIoU losses as in DETR-like methods [9, 34, 37, 41, 74, 75]. L_{RA} denotes referent alignment loss, L_{center} indicates object center prediction loss, and L_g is gesture prediction loss. L_t and L_c are soft token loss and contrastive loss respectively to help visual and textural signals alignment as in [30]. We empirically determine the optimal coefficients on the validation set (See Appendix E).

4. Experimental Results

Dataset For both training and testing, we use the image subset of the YouRefIt dataset [11], as the video portion is not publicly available. The dataset contains 2,950 training images and 1,245 test images. Annotations for bounding boxes, as well as eye, fingertip, elbow, and wrist coordinates, are provided by [11, 35].

Evaluation For fair evaluation and comparison, we follow prior work [11] and report mean Average Precision

IoU Threshold for mAP	0.25				0.50				0.75			
Object Sizes	All	S	M	L	All	S	M	L	All	S	M	L
Grounding DINO [37]	57.9	38.0	60.9	74.9	54.9	35.7	59.3	69.6	42.3	22.7	45.9	58.4
FAOA [69]	44.5	30.6	48.6	54.1	30.4	15.8	36.5	39.3	8.5	1.4	9.6	14.4
ReSC [70]	49.2	32.3	54.7	60.1	34.9	14.1	42.5	47.7	10.5	0.2	10.6	20.1
YourRefit PAF [11]	52.6	35.9	60.5	61.4	37.6	14.6	49.1	49.1	12.7	1.0	16.5	20.5
YourRefit Full [11]	54.7	38.5	64.1	61.6	40.5	16.3	54.4	51.1	14.0	1.2	17.2	23.3
REP [52]	58.8	44.7	68.9	63.2	45.7	25.4	57.7	54.3	18.8	3.8	22.2	29.9
Touch-Line-EWL [35]	69.5	56.6	71.7	80.0	60.7	44.4	66.2	71.2	35.5	11.8	38.9	55.0
Touch-Line-VTL [35]	71.1	55.9	75.5	81.7	63.5	47.0	70.2	73.1	<u>39.0</u>	<u>13.4</u>	<u>45.2</u>	<u>57.8</u>
Ours (CAPE)	75.0	63.2	80.2	81.8	65.4	49.5	74.3	<u>72.7</u>	35.7	<u>13.4</u>	40.1	53.5

Table 1. Comparison of our model with prior work in terms of mean Average Precision (mAP) at different IoU thresholds, across various object sizes, on the YouRefIt dataset [11].

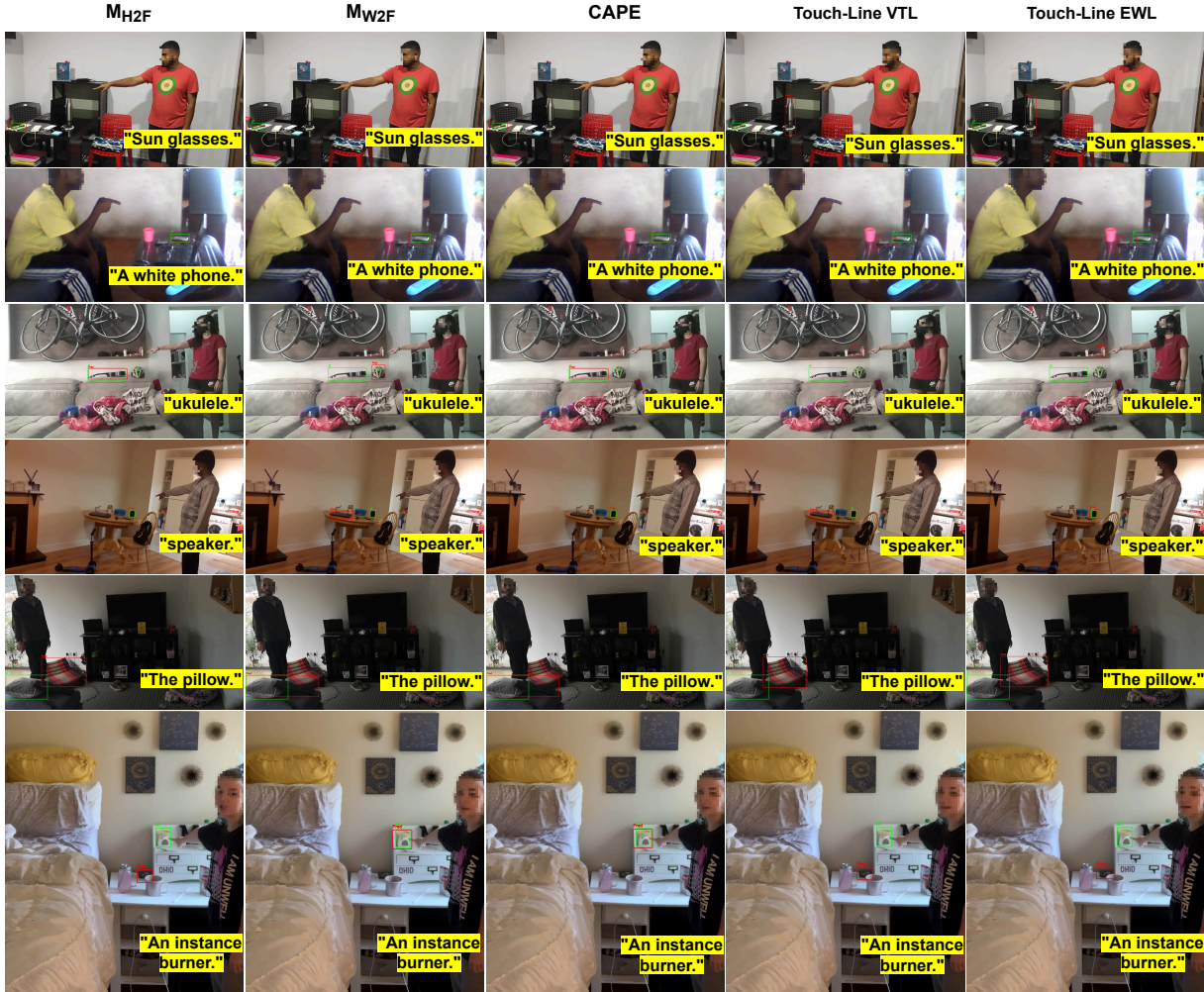


Figure 3. Sample images and predictions with our models as well as recent SOTA Touch-Line Transformer [35].

(mAP) under three Intersection-over-Union (IoU) thresholds: 0.25, 0.50, and 0.75. A prediction is considered correct if its IoU with the GT exceeds the given threshold. Ad-

ditionally, by following the literature, mAP scores are reported with respect to object size, categorized as Small (S), Medium (M), and Large (L). The object size categories are

determined based on the ratio of the object area to the image area, using two thresholds [11]: 0.48% and 1.76%. An object is classified as small if its area ratio is below 0.48%, medium if it falls between 0.48% and 1.76%, and large otherwise. In addition to this standard evaluation protocol, we introduce two metrics for assessing referential grounding performance: CLIP score and center coordinate distance (C_D). To compute the CLIP score, we extract features from the text input and the cropped region corresponding to the predicted bounding box using CLIP’s text and image encoders. We then calculate the cosine similarity between these feature vectors to quantify the semantic alignment between the predicted object and the text. For C_D , we compute the L1 distance between the center coordinates of the predicted bounding box and those of the GT bounding box, providing a direct measure of spatial alignment.

Implementation We use the AMSGrad optimizer [32, 49] during training and train our models for 30 epochs. Both the transformer encoder and decoder consist of 6 layers, each with 8 attention heads and an MLP dimension of 2048. We apply dropout [54] with $p = 0.1$ in every layer of both the transformer encoder and decoder. The learning rate is set to $1e - 4$ for the text encoder and $5e - 5$ for the remaining components. All experiments are conducted on a single NVIDIA RTX A6000 GPU with a batch size of 4.

Objet Sizes	CLIP Score \uparrow				$C_D \downarrow$			
	All	S	M	L	All	S	M	L
Touch-Line-EWL	0.7369	0.6936	0.7305	0.7845	0.3168	0.3006	0.2903	0.3564
Touch-Line-VTL	0.7368	0.6925	0.7321	0.7846	0.2843	0.2809	0.2276	0.3393
Ours	0.7983	0.7927	0.8015	0.8010	0.2476	0.2137	0.2241	0.3023

Table 2. Clip score and C_D metric with respect to the object size.

4.1. Results

Tab. 1 compares the performance of our method with existing approaches on the YouRefIt benchmark. Our model achieves SOTA results across all objects at IoU thresholds of 0.25 and 0.50, despite being trained for only 30 epochs on a single GPU with a batch size of 4. According to our experiments, this limited training setup affects bounding box precision, contributing to the suboptimal performance at $IoU = 0.75$, alongside limitations related to the backbone (see Grounding DINO in Tab. 1 for backbone). In contrast, Touch-Line [35] was trained for 200 epochs with a batch size of 56. This clearly demonstrates the efficiency and effectiveness of our approach. Tab. 2 presents a comparison between our method and the previous SOTA, Touch-Line, using two new metrics in this field: CLIP score and C_D . The higher CLIP scores indicate that our predicted bounding boxes have stronger semantic alignment with the input text, suggesting better object identification and improved

bounding box precision. Similarly, our method achieves the best performance under the C_D metric, which quantifies the distance between the centers of the predicted and GT bounding boxes. This confirms that our model produces more spatially accurate predictions. In Fig. 3, we present samples images with predicted and GT bounding boxes. We compare our model with Touch-Line [35].

Setup	Method	IoU=0.25	IoU=0.5	IoU=0.75	CLIP \uparrow	$C_D \downarrow$
A	Baseline	71.2	60.1	32.8	0.7409	0.2662
B	A + object center prediction	70.8	61.6	34.6	0.7339	0.2707
C	A + W2F heatmap	68.9	59.7	32.4	0.7353	0.2984
D	A + H2F heatmap	71.9	62.8	33.8	0.7375	0.2694
E	B + W2F heatmap (M_{W2F})	69.6	60.7	31.5	0.7344	0.2770
F	B + H2F heatmap (M_{H2F})	72.9	62.3	35.1	0.7373	0.2490
G	A + W2F heatmap + H2F heatmap	70.2	60.2	33.8	0.7345	0.2744
H	Full model - Ensemble of E and F	75.0	65.4	35.7	0.7983	0.2476

Table 3. Ablation study for object center prediction and heatmaps.

4.2. Analysis

In this section, we provide a detailed analysis of the optimality of our design choices, including heatmap generation and the ensemble method. Specifically, we examine various heatmap injection strategies and ensemble approaches, among other factors. The baseline in Tab. 3 (Setup A) refers to a straightforward training of our model without incorporating any of the proposed contributions.

Object center prediction The object center prediction head and its associated loss yield improvements over the baseline in terms of mAP at $IoU = 0.5$ and $IoU = 0.75$. However, they have a detrimental effect on mAP at $IoU = 0.25$, as well as on the CLIP Score and C_D . Notably, when combined with the heatmap (Setup E and F in Tab. 3), we observe improvements across most metrics (see comparisons from Setup C to E and from Setup D to F).

	IoU=0.25	IoU=0.5	IoU=0.75	CLIP \uparrow	$C_D \downarrow$
Channel-wise input	68.7	58.5	33.4	0.7348	0.2959
Channel-wise feature	72.6	58.4	27.9	0.7372	0.2598
Embedding feature	72.9	62.2	35.1	0.7373	0.2490

Table 4. Comparison of heatmap injection methods using Setup F.

Where to inject heatmap We explore various methods for incorporating the heatmap into the model and present the results in Tab. 4. First, we examine the *channel-wise input* approach, which involves concatenating the heatmap with the input image and feeding a 4-channel input into the image encoder. However, this method leads to a slight drop in performance. This is likely because the image encoder struggles to extract meaningful supervision from the fourth channel, as the heatmap is sparsely represented compared

to the image content. In the second approach, *channel-wise feature*, we adopt the head prompting strategy proposed in [51]. Specifically, we use an embedding layer to learn heatmap embeddings, which are then added to the visual tokens. While this method is computationally efficient and does not require retraining the image encoder, the resulting performance improvement for our task is minimal. Finally, in the *embedding feature* setup, we introduce an additional CNN-based encoder to process the heatmap. The resulting heatmap embedding is passed through a projection head and then concatenated with the image and text embeddings before being fed into the transformer encoder. This approach yields the most substantial performance improvement among the methods evaluated.

Ensemble method	IoU=0.25	IoU=0.5	IoU=0.75	CLIP \uparrow	$C_D \downarrow$
Confidence-Only	73.4	64.1	34.1	0.7735	0.2470
CLIP-Only (Top-1)	73.5	64.2	35.4	0.7932	0.2391
CLIP-Only (Top-2 + Threshold=0.95)	73.8	64.1	35.5	0.7938	0.2377
CLIP Fusion	73.6	64.4	34.5	0.7379	0.2422
CAPE	75.0	65.4	35.7	0.7983	0.2476

Table 5. Comparison of different ensemble methods. See Appendix C for more details.

CLIP-Aware Pointing Ensemble (CAPE) We evaluate several ensemble strategies to determine the final referent bounding box from the outputs of the two pointing models and present the results in Tab. 5. (1) *Confidence-Only*: selects the box with the highest model confidence score among Top-1 prediction of both models. (2) *CLIP-Only (Top-1)*: chooses the box with the highest CLIP similarity score between the text and Top-1 predictions from both models. (3) *CLIP-Only (Top-2 + Threshold= 0.95)*: extends the previous method by also considering the top-2 predictions from each model, provided their confidence scores exceed 0.95. (4) *CLIP Fusion*: computes a normalized CLIP score and sums it with the model’s confidence score. The box with the highest total score is selected. This method considers the top-2 predictions from both models. (5) *CAPE*: a hybrid method that combines approaches (3) and (4). For small objects, defined by [11] as occupying less than 0.48% of the image area, CAPE uses method (4), since CLIP tends to perform unreliably on very small referents. For all other objects, it uses method (3). This adaptive strategy balances the strengths of both scoring signals across varying object sizes. Please note that the threshold used in method (3), as well as the decision to apply method (4) for small objects, were determined based on performance analysis on the validation set to avoid overfitting to the test set.

Finetuned vs. frozen text encoder We investigate the impact of freezing the text encoder during training. While freezing the text encoder reduces computational cost, miti-

gates overfitting in low-resource settings, and stabilizes the training (see Appendix D), we observe that finetuning consistently yields better performance across almost all evaluation metrics (see Tab. 6). This suggests that adapting the text features to the specific task of embodied reference understanding provides a meaningful benefit.

Text Encoder	IoU=0.25	IoU=0.5	IoU=0.75	CLIP \uparrow	$C_D \downarrow$
Frozen, Setup A	69.8	59.5	33.1	0.7363	0.2994
Finetuned, Setup A	71.2	60.1	32.8	0.7409	0.2662
Frozen, Setup F	71.3	62.1	33.7	0.7382	0.2634
Finetuned, Setup F	72.9	62.2	35.1	0.7373	0.2490

Table 6. Ablation study for text encoder. Although frozen text encoder setup demonstrates more stable training and early converge, finetuning text encoder yields enhanced performance.

How to create heatmap We evaluate the Conic Attention Heatmap with 15° and 30° cone angles, as well as the Gaussian Ray Heatmap, which yields a more localized activation. Empirically, the Gaussian Ray Heatmap achieved the best performance (see Tab. 7). This suggests that broader attention regions may be less effective for the model, likely due to the high density of objects in typical scenes. Therefore, larger heatmaps tend to enclose multiple distractors, reducing the discriminative value of the spatial signal.

Heatmap style	IoU=0.25	IoU=0.5	IoU=0.75	CLIP \uparrow	$C_D \downarrow$
Gaussian Ray Heatmap ($\sigma = 25$)	72.9	62.2	35.1	0.7373	0.2490
Conic Attention Heatmap (15°)	70.0	60.0	33.9	0.7392	0.2632
Conic Attention Heatmap (30°)	71.5	59.4	30.8	0.7389	0.2764

Table 7. Comparison of different heatmap generation approaches.

5. Conclusion

We tackled the challenge of Embodied Reference Understanding by addressing the limitations of existing single-line pointing assumptions. Our proposed dual-model framework explicitly leverages both head-to-fingertip and wrist-to-fingertip lines, represented as Gaussian ray heatmaps, to provide richer supervision beyond following pointing line and improve pointing target detection. By integrating these complementary signals through our CLIP-Aware Pointing Ensemble (CAPE) module and enhancing the model with an auxiliary object center prediction task, we achieve notable improvements on the YouRefIt benchmark. Our results demonstrate that combining multiple pointing cues and multimodal signals leads to more accurate and robust referent understanding in complex visual scenes.

Limitations Due to the lack of explicit depth information, the model occasionally selects an incorrect object that lies

along the pointing direction but is not the intended referent. We plan to address this depth-related issue in future work. Additionally, the use of a CNN-based image backbone leads to suboptimal precision in bounding box predictions. This limitation can be mitigated by adopting a more advanced backbone architecture, such as the Swin Transformer.

References

- [1] Marah Abdin, Jyoti Aneja, Harkirat Behl, Sébastien Bubeck, Ronen Eldan, Suriya Gunasekar, Michael Harrison, Russell J Hewett, Mojan Javaheripi, Piero Kauffmann, et al. Phi-4 technical report. *arXiv preprint arXiv:2412.08905*, 2024. 2
- [2] Nada H Alalyani. *Embodied Multimodal Referring Expressions Generation*. PhD thesis, Colorado State University, 2024. 2
- [3] Jinze Bai, Shuai Bai, Shusheng Yang, Shijie Wang, Sinan Tan, Peng Wang, Junyang Lin, Chang Zhou, and Jingren Zhou. Qwen-vl: A frontier large vision-language model with versatile abilities. *arXiv preprint arXiv:2308.12966*, 1(2):3, 2023. 2
- [4] Loris Bazzani, Marco Cristani, Diego Tosato, Michela Farenzena, Giulia Paggetti, Gloria Menegaz, and Vittorio Murino. Social interactions by visual focus of attention in a three-dimensional environment. *Expert Systems*, 30(2):115–127, 2013. 2
- [5] Lucas Beyer, Andreas Steiner, André Susano Pinto, Alexander Kolesnikov, Xiao Wang, Daniel Salz, Maxim Neumann, Ibrahim Alabdulmohsin, Michael Tschannen, Emanuele Bugliarello, et al. Paligemma: A versatile 3b vlm for transfer. *arXiv preprint arXiv:2407.07726*, 2024. 2
- [6] Brice Burger, Isabelle Ferrané, Frédéric Lerasle, and Guillaume Infantes. Two-handed gesture recognition and fusion with speech to command a robot. *Autonomous Robots*, 32(2):129–147, 2012. 2
- [7] Zhe Cao, Tomas Simon, Shih-En Wei, and Yaser Sheikh. Realtime multi-person 2d pose estimation using part affinity fields. In *Proceedings of the IEEE conference on computer vision and pattern recognition*, pages 7291–7299, 2017. 2
- [8] Francesca Capozzi, Cigdem Beyan, Antonio Pierro, Atesh Koul, Vittorio Murino, Stefano Livi, Andrew P Bayliss, Jelena Ristic, and Cristina Becchio. Tracking the leader: Gaze behavior in group interactions. *Iscience*, 16:242–249, 2019. 2
- [9] Nicolas Carion, Francisco Massa, Gabriel Synnaeve, Nicolas Usunier, Alexander Kirillov, and Sergey Zagoruyko. End-to-end object detection with transformers. In *European conference on computer vision*, pages 213–229. Springer, 2020. 2, 5
- [10] Jierun Chen, Fangyun Wei, Jinjing Zhao, Sizhe Song, Bohuai Wu, Zhuoxuan Peng, S-H Gary Chan, and Hongyang Zhang. Revisiting referring expression comprehension evaluation in the era of large multimodal models. In *Proceedings of the Computer Vision and Pattern Recognition Conference*, pages 513–524, 2025. 2
- [11] Yixin Chen, Qing Li, Deqian Kong, Yik Lun Kei, Song-Chun Zhu, Tao Gao, Yixin Zhu, and Siyuan Huang. Yourefit: Embodied reference understanding with language and gesture. In *Proceedings of the IEEE/CVF International Conference on Computer Vision*, pages 1385–1395, 2021. 1, 2, 5, 6, 7, 8, 4
- [12] Tianheng Cheng, Lin Song, Yixiao Ge, Wenyu Liu, Xingang Wang, and Ying Shan. Yolo-world: Real-time open-vocabulary object detection. In *Proceedings of the IEEE/CVF conference on computer vision and pattern recognition*, pages 16901–16911, 2024. 2
- [13] Jaemin Cho, Jie Lei, Hao Tan, and Mohit Bansal. Unifying vision-and-language tasks via text generation. In *International Conference on Machine Learning*, pages 1931–1942. PMLR, 2021. 2
- [14] Stefan Constantin, Fevziye Irem Eyiokur, Dogucan Yaman, Leonard Börmann, and Alex Waibel. Interactive multimodal robot dialog using pointing gesture recognition. In *European conference on computer vision*, pages 640–657. Springer, 2022. 2
- [15] Stefan Constantin, Fevziye Irem Eyiokur, Dogucan Yaman, Leonard Börmann, and Alex Waibel. Multimodal error correction with natural language and pointing gestures. In *Proceedings of the IEEE/CVF International Conference on Computer Vision*, pages 1976–1986, 2023. 2
- [16] Jacob Devlin, Ming-Wei Chang, Kenton Lee, and Kristina Toutanova. Bert: Pre-training of deep bidirectional transformers for language understanding. In *Proceedings of the 2019 conference of the North American chapter of the association for computational linguistics: human language technologies, volume 1 (long and short papers)*, pages 4171–4186, 2019. 3
- [17] Peng Gao, Shijie Geng, Renrui Zhang, Teli Ma, Rongyao Fang, Yongfeng Zhang, Hongsheng Li, and Yu Qiao. Clip-adapter: Better vision-language models with feature adapters. *International Journal of Computer Vision*, 132(2): 581–595, 2024. 2
- [18] Ross Girshick, Jeff Donahue, Trevor Darrell, and Jitendra Malik. Rich feature hierarchies for accurate object detection and semantic segmentation. In *Proceedings of the IEEE conference on computer vision and pattern recognition*, pages 580–587, 2014. 2
- [19] Xiuye Gu, Tsung-Yi Lin, Weicheng Kuo, and Yin Cui. Open-vocabulary object detection via vision and language knowledge distillation. *arXiv preprint arXiv:2104.13921*, 2021. 2
- [20] Anshul Gupta, Samy Tafasca, and Jean-Marc Odobez. A modular multimodal architecture for gaze target prediction: Application to privacy-sensitive settings. In *Proceedings of the IEEE/CVF Conference on Computer Vision and Pattern Recognition*, pages 5041–5050, 2022. 2
- [21] Anshul Gupta, Pierre Vuillecard, Arya Farkhondeh, and Jean-Marc Odobez. Exploring the zero-shot capabilities of vision-language models for improving gaze following. In *Proceedings of the IEEE/CVF conference on computer vision and pattern recognition*, pages 615–624, 2024. 2
- [22] Kaiming He, Xiangyu Zhang, Shaoqing Ren, and Jian Sun. Deep residual learning for image recognition. In *Proceedings of the IEEE conference on computer vision and pattern recognition*, pages 770–778, 2016. 3

- [23] Shuting He, Henghui Ding, Chang Liu, and Xudong Jiang. Grec: Generalized referring expression comprehension. *arXiv preprint arXiv:2308.16182*, 2023. 2
- [24] Oliver Herbolt and Wilfried Kunde. How to point and to interpret pointing gestures? instructions can reduce pointer–observer misunderstandings. *Psychological research*, 82(2): 395–406, 2018. 2
- [25] Hartwig Holzapfel, Kai Nickel, and Rainer Stiefelhagen. Implementation and evaluation of a constraint-based multi-modal fusion system for speech and 3d pointing gestures. In *Proceedings of the 6th international conference on Multi-modal interfaces*, pages 175–182, 2004. 2
- [26] Md Mofijul Islam, Reza Mirzaiee, Alexi Gladstone, Haley Green, and Tariq Iqbal. Caesar: An embodied simulator for generating multimodal referring expression datasets. *Advances in Neural Information Processing Systems*, 35: 21001–21015, 2022. 2
- [27] Md Mofijul Islam, Alexi Gladstone, Riashat Islam, and Tariq Iqbal. Eqa-mx: Embodied question answering using multi-modal expression. In *The Twelfth International Conference on Learning Representations*, 2023.
- [28] Aman Jain, Teruhisa Misu, Kentaro Yamada, and Hitomi Yanaka. Gesnavi: gesture-guided outdoor vision-and-language navigation. In *Proceedings of the 18th Conference of the European Chapter of the Association for Computational Linguistics: Student Research Workshop*, pages 290–295, 2024. 2
- [29] Kritika Johari, Christopher Tay Zi Tong, Vigneshwaran Subbaraju, Jung-Jae Kim, and U-Xuan Tan. Gaze assisted visual grounding. In *International Conference on Social Robotics*, pages 191–202. Springer, 2021. 2
- [30] Aishwarya Kamath, Mannat Singh, Yann LeCun, Gabriel Synnaeve, Ishan Misra, and Nicolas Carion. Mdetrm: modulated detection for end-to-end multi-modal understanding. In *Proceedings of the IEEE/CVF international conference on computer vision*, pages 1780–1790, 2021. 2, 3, 5
- [31] Sahar Kazemzadeh, Vicente Ordonez, Mark Matten, and Tamara Berg. Referitgame: Referring to objects in photographs of natural scenes. In *Proceedings of the 2014 conference on empirical methods in natural language processing (EMNLP)*, pages 787–798, 2014. 2
- [32] Diederik P Kingma and Jimmy Ba. Adam: A method for stochastic optimization. *arXiv preprint arXiv:1412.6980*, 2014. 7
- [33] Alexander Kroner, Mario Senden, Kurt Driessens, and Rainer Goebel. Contextual encoder–decoder network for visual saliency prediction. *Neural Networks*, 129:261–270, 2020. 2
- [34] Feng Li, Hao Zhang, Shilong Liu, Jian Guo, Lionel M Ni, and Lei Zhang. Dn-detr: Accelerate detr training by introducing query denoising. In *Proceedings of the IEEE/CVF conference on computer vision and pattern recognition*, pages 13619–13627, 2022. 5
- [35] Yang Li, Xiaoxue Chen, Hao Zhao, Jiangtao Gong, Guyue Zhou, Federico Rossano, and Yixin Zhu. Understanding embodied reference with touch-line transformer. In *The Eleventh International Conference on Learning Representations*, 2023. 2, 3, 5, 6, 7, 1
- [36] Tsung-Yi Lin, Michael Maire, Serge Belongie, James Hays, Pietro Perona, Deva Ramanan, Piotr Dollár, and C Lawrence Zitnick. Microsoft coco: Common objects in context. In *European conference on computer vision*, pages 740–755. Springer, 2014. 2
- [37] Shilong Liu, Zhaoyang Zeng, Tianhe Ren, Feng Li, Hao Zhang, Jie Yang, Qing Jiang, Chunyuan Li, Jianwei Yang, Hang Su, et al. Grounding dino: Marrying dino with grounded pre-training for open-set object detection. In *European conference on computer vision*, pages 38–55. Springer, 2024. 1, 2, 5, 6
- [38] Yinhan Liu, Myle Ott, Naman Goyal, Jingfei Du, Mandar Joshi, Danqi Chen, Omer Levy, Mike Lewis, Luke Zettlemoyer, and Veselin Stoyanov. Roberta: A robustly optimized bert pretraining approach. *arXiv preprint arXiv:1907.11692*, 2019. 3
- [39] Ziyang Lu, Yunqiang Pei, Guoqing Wang, Peiwei Li, Yang Yang, Yinjie Lei, and Heng Tao Shen. Scaneru: Interactive 3d visual grounding based on embodied reference understanding. In *Proceedings of the AAAI Conference on Artificial Intelligence*, pages 3936–3944, 2024. 3
- [40] Atharv Mahesh Mane, Dulanga Weerakoon, Vigneshwaran Subbaraju, Sougata Sen, Sanjay E Sarma, and Archan Misra. Ges3vig: Incorporating pointing gestures into language-based 3d visual grounding for embodied reference understanding. In *Proceedings of the Computer Vision and Pattern Recognition Conference*, pages 9017–9026, 2025. 3
- [41] Depu Meng, Xiaokang Chen, Zejia Fan, Gang Zeng, Houqiang Li, Yuhui Yuan, Lei Sun, and Jingdong Wang. Conditional detr for fast training convergence. In *Proceedings of the IEEE/CVF international conference on computer vision*, pages 3651–3660, 2021. 5
- [42] Varun K Nagaraja, Vlad I Morariu, and Larry S Davis. Modeling context between objects for referring expression understanding. In *European Conference on Computer Vision*, pages 792–807. Springer, 2016. 2
- [43] Akira Oyama, Shoichi Hasegawa, Hikaru Nakagawa, Akira Taniguchi, Yoshinobu Hagiwara, and Tadahiro Taniguchi. Exophora resolution of linguistic instructions with a demonstrative based on real-world multimodal information. In *2023 32nd IEEE International Conference on Robot and Human Interactive Communication (RO-MAN)*, pages 2617–2623. IEEE, 2023. 2
- [44] Cathal O’madagain, Gregor Kachel, and Brent Strickland. The origin of pointing: Evidence for the touch hypothesis. *Science Advances*, 5(7):eaav2558, 2019. 2
- [45] Maria Pateraki, Haris Baltzakis, and Panos Trahanias. Visual estimation of pointed targets for robot guidance via fusion of face pose and hand orientation. *Computer Vision and Image Understanding*, 120:1–13, 2014. 2
- [46] Renjie Pi, Lewei Yao, Jiahui Gao, Jipeng Zhang, and Tong Zhang. Perceptiongpt: Effectively fusing visual perception into llm. In *Proceedings of the IEEE/CVF conference on computer vision and pattern recognition*, pages 27124–27133, 2024. 2
- [47] Yanyuan Qiao, Chaorui Deng, and Qi Wu. Referring expression comprehension: A survey of methods and datasets. *IEEE Transactions on Multimedia*, 23:4426–4440, 2020. 2

- [48] Alec Radford, Jong Wook Kim, Chris Hallacy, Aditya Ramesh, Gabriel Goh, Sandhini Agarwal, Girish Sastry, Amanda Askell, Pamela Mishkin, Jack Clark, et al. Learning transferable visual models from natural language supervision. In *International conference on machine learning*, pages 8748–8763. PmLR, 2021. 4
- [49] Sashank J Reddi, Satyen Kale, and Sanjiv Kumar. On the convergence of adam and beyond. *arXiv preprint arXiv:1904.09237*, 2019. 7
- [50] Joseph Redmon, Santosh Divvala, Ross Girshick, and Ali Farhadi. You only look once: Unified, real-time object detection. In *Proceedings of the IEEE conference on computer vision and pattern recognition*, pages 779–788, 2016. 2
- [51] Fiona Ryan, Ajay Bati, Sangmin Lee, Daniel Bolya, Judy Hoffman, and James M Rehg. Gaze-llc: Gaze target estimation via large-scale learned encoders. In *Proceedings of the Computer Vision and Pattern Recognition Conference*, pages 28874–28884, 2025. 2, 8
- [52] Cheng Shi and Sibe Yang. Spatial and visual perspective-taking via view rotation and relation reasoning for embodied reference understanding. In *European Conference on Computer Vision*, pages 201–218. Springer, 2022. 2, 6
- [53] Kevin Smith, Sileye O Ba, Jean-Marc Odobez, and Daniel Gatica-Perez. Tracking the visual focus of attention for a varying number of wandering people. *IEEE transactions on pattern analysis and machine intelligence*, 30(7):1212–1229, 2008. 2
- [54] Nitish Srivastava, Geoffrey Hinton, Alex Krizhevsky, Ilya Sutskever, and Ruslan Salakhutdinov. Dropout: a simple way to prevent neural networks from overfitting. *The journal of machine learning research*, 15(1):1929–1958, 2014. 7
- [55] Rainer Stiefelhagen, Michael Finke, Jie Yang, and Alex Waibel. From gaze to focus of attention. In *International Conference on Advances in Visual Information Systems*, pages 765–772. Springer, 1999. 2
- [56] Rainer Stiefelhagen, Jie Yang, and Alex Waibel. Estimating focus of attention based on gaze and sound. In *Proceedings of the 2001 workshop on Perceptive user interfaces*, pages 1–9, 2001.
- [57] Rainer Stiefelhagen, Christian Fugen, R Gieselmann, Hartwig Holzapfel, Kai Nickel, and Alex Waibel. Natural human-robot interaction using speech, head pose and gestures. In *2004 IEEE/RSJ international conference on intelligent robots and systems (IROS)(IEEE cat. no. 04CH37566)*, pages 2422–2427. IEEE, 2004.
- [58] Samy Tafasca, Anshul Gupta, and Jean-Marc Odobez. Child-play: A new benchmark for understanding children’s gaze behaviour. In *Proceedings of the IEEE/CVF International Conference on Computer Vision*, pages 20935–20946, 2023.
- [59] Samy Tafasca, Anshul Gupta, Victor Bros, and Jean-Marc Odobez. Toward semantic gaze target detection. *Advances in neural information processing systems*, 37:121422–121448, 2024.
- [60] Samy Tafasca, Anshul Gupta, and Jean-Marc Odobez. Sharingan: A transformer architecture for multi-person gaze following. In *Proceedings of the IEEE/CVF conference on computer vision and pattern recognition*, pages 2008–2017, 2024.
- [61] Kosei Tanada, Shigemichi Matsuzaki, Kazuhito Tanaka, Shintaro Nakaoka, Yuki Kondo, and Yuto Mori. Pointing gesture understanding via visual prompting and visual question answering for interactive robot navigation. In *First Workshop on Vision-Language Models for Navigation and Manipulation at ICRA 2024*, 2024.
- [62] Francesco Tonini, Cigdem Beyan, and Elisa Ricci. Multi-modal across domains gaze target detection. In *Proceedings of the 2022 International Conference on Multimodal Interaction*, pages 420–431, 2022.
- [63] Francesco Tonini, Nicola Dall’Asen, Cigdem Beyan, and Elisa Ricci. Object-aware gaze target detection. In *Proceedings of the IEEE/CVF international conference on computer vision*, pages 21860–21869, 2023.
- [64] Roberto Valenti, Nicu Sebe, and Theo Gevers. Combining head pose and eye location information for gaze estimation. *IEEE Transactions on Image Processing*, 21(2):802–815, 2011. 2
- [65] Ashish Vaswani, Noam Shazeer, Niki Parmar, Jakob Uszkoreit, Llion Jones, Aidan N Gomez, Łukasz Kaiser, and Illia Polosukhin. Attention is all you need. *Advances in neural information processing systems*, 30, 2017. 3
- [66] Yang Xiao, Zhijun Zhang, Aryel Beck, Junsong Yuan, and Daniel Thalmann. Human–robot interaction by understanding upper body gestures. *Presence*, 23(2):133–154, 2014. 2
- [67] Hee-Deok Yang, A-Yeon Park, and Seong-Whan Lee. Gesture spotting and recognition for human–robot interaction. *IEEE Transactions on robotics*, 23(2):256–270, 2007.
- [68] Yaokun Yang and Feng Lu. Gaze target detection based on head-local-global coordination. In *European Conference on Computer Vision*, pages 305–322. Springer, 2024. 2
- [69] Zhengyuan Yang, Boqing Gong, Liwei Wang, Wenbing Huang, Dong Yu, and Jiebo Luo. A fast and accurate one-stage approach to visual grounding. In *Proceedings of the IEEE/CVF international conference on computer vision*, pages 4683–4693, 2019. 6
- [70] Zhengyuan Yang, Tianlang Chen, Liwei Wang, and Jiebo Luo. Improving one-stage visual grounding by recursive subquery construction. In *European conference on computer vision*, pages 387–404. Springer, 2020. 6
- [71] Lewei Yao, Jianhua Han, Youpeng Wen, Xiaodan Liang, Dan Xu, Wei Zhang, Zhenguo Li, Chunjing Xu, and Hang Xu. Detclip: Dictionary-enriched visual-concept paralleled pre-training for open-world detection. *Advances in Neural Information Processing Systems*, 35:9125–9138, 2022. 2
- [72] Licheng Yu, Zhe Lin, Xiaohui Shen, Jimei Yang, Xin Lu, Mohit Bansal, and Tamara L Berg. Mattnet: Modular attention network for referring expression comprehension. In *Proceedings of the IEEE conference on computer vision and pattern recognition*, pages 1307–1315, 2018. 2
- [73] Alireza Zareian, Kevin Dela Rosa, Derek Hao Hu, and Shih-Fu Chang. Open-vocabulary object detection using captions. In *Proceedings of the IEEE/CVF conference on computer vision and pattern recognition*, pages 14393–14402, 2021. 2
- [74] Hao Zhang, Feng Li, Shilong Liu, Lei Zhang, Hang Su, Jun Zhu, Lionel M Ni, and Heung-Yeung Shum. Dino: Detr with improved denoising anchor boxes for end-to-end object detection. *arXiv preprint arXiv:2203.03605*, 2022. 5

- [75] Xizhou Zhu, Weijie Su, Lewei Lu, Bin Li, Xiaogang Wang, and Jifeng Dai. Deformable detr: Deformable transformers for end-to-end object detection. *arXiv preprint arXiv:2010.04159*, 2020. [5](#)

CAPE: A CLIP-Aware Pointing Ensemble of Complementary Heatmap Cues for Embodied Reference Understanding

Supplementary Material

A. Problem Analysis

How important is ERU task? Embodied Reference Understanding (ERU) is a challenging multimodal task that combines visual, linguistic, and embodied cues (like gestures / pointing) to predict a target object in a scene. Despite recent progress, several key problems and open challenges remain. Natural language instructions are often vague or underspecified. Therefore, grounding models may detect multiple candidate objects or fail to resolve the correct referent altogether. Another problem is that when multiple instances of the same object class exist, models struggle to disambiguate. This results in over-detection (selecting all candidates) or under-confidence in selecting the target.

YouRefIt [11] introduced the ERU task, along with a multimodal dataset and a baseline approach to address it. However, the proposed method demonstrated limited performance, achieving a mean Average Precision (mAP) of only 0.58 under an IoU threshold of 0.25. Subsequently, Touch-Line Transformer [35] proposed the concept of a Virtual Touch Line (VTL), based on the observation that the referent is typically aligned with the head-to-fingertip (H2F) line rather than the elbow-to-wrist (E2W) line. Since models struggle to follow pointing instructions, they propose using VTL prediction with a dedicated prediction head to encourage the model to focus more on the corresponding line. This approach led to a significant improvement in performance. However, our empirical analysis confirms that while the referent often aligns with the head-to-fingertip line, this is not always the case due to several factors:

- If the person is looking elsewhere, such as at the camera, a robot, or another person, the alignment no longer holds.
- The camera angle, consequently the image perspective, affects this alignment.
- If the person is very close to the object or does not fully extend their arm while pointing the alignment may again be lost.

As a result, we find that in some cases, the referent aligns with the wrist-to-fingertip line. This indicates the need to incorporate both sources of information either in model training or decision step.

B. Heatmap Generation

The heatmap generation method is a critical component of our approach. Recent work in this field [35] has shown that the referent often aligns with the head-to-fingertip line, referred to as the Virtual Touch-Line (VTL). Based on this in-

sight, we generate a Gaussian Ray Heatmap using the head-to-fingertip line as a reference. While this assumption generally holds true, particularly when a person clearly points toward an object with an extended arm, it is not universally reliable. Variations occur both in this benchmark and in real-world scenarios. For instance, the alignment may be disrupted if the person is looking elsewhere (e.g., at a robot, camera, or another person). Similarly, camera perspective can also distort the alignment. In some cases, we observe that the wrist-to-fingertip line aligns more accurately with the referent than the head-to-fingertip line. To address this variability, we leverage both types of information and generate separate heatmaps for each sample accordingly.

- x_{phm}^{H2F} : Heatmap from head-to-fingertip.
- x_{phm}^{W2F} : Heatmap from wrist-to-fingertip.

B.1. Head-to-Fingertip Heatmap

To generate this heatmap, we use the head and fingertip as reference points to draw a line starting from the head and extending toward the edge of the image in the direction of the fingertip. In the YouRefIt dataset [11], we have access to detailed annotations from [11, 35], which include coordinates for the eyes, elbows, wrists, and fingertips. We utilize these annotations to construct the reference line and generate the corresponding heatmap. In real-world applications where such annotations are not available, estimating these key points is straightforward. For the eye position, face detection followed by selecting the center point of the detected face yields comparable performance. Likewise, for wrist and fingertip locations, modern pose estimation models provide reliable predictions.

B.2. Wrist-to-Fingertip Heatmap

We follow the same pipeline used for generating the head-to-fingertip heatmap, but replace the eye coordinates with wrist coordinates and the fingertip coordinates remain the same.

B.3. Merging

For the unimodal experiments, we merge the head-to-fingertip and wrist-to-fingertip heatmaps to combine information from different pointing directions. However, this approach yields lower accuracy compared to using two separate models. We hypothesize that this is primarily because the model cannot inherently determine which pointing line is more appropriate for each sample.

B.4. Heatmap Injection Methods

We investigate three different methods for injecting heatmaps and conduct experiments using the head-to-fingertip heatmap.

Channel-wise input In this method, we concatenate the input image with the heatmap and feed it into the image encoder, resulting in a 4-channel input. Consequently, this approach is not compatible with pretrained image encoders unless they are finetuned, as it requires adapting the model to handle the additional channel. Experimental results show that this method yields the least accurate performance.

Channel-wise feature In this method, we follow a recently proposed approach [51] that has shown strong performance in the gaze target estimation literature. Specifically, we use a single learnable embedding layer to obtain embeddings of the heatmap, which are then added to the image embeddings.

Embedding feature In this approach, we propose using an additional encoder. Given the sparse nature of the heatmap representation, we select a simpler encoder than the main image encoder. In this work, we employ ResNet-18 as the heatmap encoder. After obtaining the embedded representation, we pass it through a projection layer to match the required dimensionality. We then concatenate it with the image and text embeddings and feed the combined representation into the transformer encoder.

C. Ensemble Methods

In this section, we present the details of the ensemble methods we explored. Each of our models produces N predictions, with each prediction accompanied by a confidence score. Before performing ensembling, we sort these N predictions in descending order based on their confidence scores. We denote the sorted prediction list from model M_{H2F} as $P_{H2F}^N \in \mathbb{R}^{4 \times N}$, and from model M_{W2F} as $P_{W2F}^N \in \mathbb{R}^{4 \times N}$. Similarly, we denote the confidence score of model M_{H2F} as $C_{H2F}^N \in \mathbb{R}^{1 \times N}$, and from model M_{W2F} as $C_{W2F}^N \in \mathbb{R}^{1 \times N}$.

C.1. Confidence-Only

In the Confidence-Only approach, we focus solely on the top-1 prediction from each model. We take the bounding box with the highest confidence score from M_{H2F} and another from M_{W2F} . These two predictions are then compared, and the one with the higher confidence score is selected as the final prediction.

Algorithm C.1 Algorithm of Confidence-Only ensembling method.

Require: Top-1 predictions from models M_{H2F} and M_{W2F} : (b^{H2F}, c^{H2F}) and (b^{W2F}, c^{W2F})

Ensure: Final bounding box prediction b^*

```

1: if  $c^{H2F} \geq c^{W2F}$  then
2:    $b^* \leftarrow b^{H2F}$ 
3: else
4:    $b^* \leftarrow b^{W2F}$ 
5: end if
6: return  $b^*$ 

```

C.2. CLIP-Only (Top-1)

In this method, similar to the Confidence-Only approach, we select the bounding box with the highest confidence score from each model. Next, we compute the CLIP similarity score between each predicted bounding box and the input text. The bounding box with the higher CLIP similarity score is then chosen as the final prediction.

$$CLIPSim_{H2F} = \max(100 * \cos(E_{I'_{H2F}}, E_T), 0) \quad (5)$$

where $E_{I'_{H2F}}$ is the embedded representation of cropped predicted bounding box of M_{H2F} with the highest score and E_T is the embedded representation of the text input.

$$CLIPSim_{W2F} = \max(100 * \cos(E_{I'_{W2F}}, E_T), 0) \quad (6)$$

where $E_{I'_{W2F}}$ is the embedded representation of cropped predicted bounding box of M_{W2F} with the highest score.

Algorithm C.2 Algorithm of CLIP-Only (Top-1) ensemble method.

Require: Top-1 predictions from models M_{H2F} and M_{W2F} : (b^{H2F}, c^{H2F}) and (b^{W2F}, c^{W2F}) , input text t

Ensure: Final bounding box prediction b^*

```

1: Crop predicted regions from  $b^{H2F}$  and  $b^{W2F}$  to get image patches  $I'_{H2F}$  and  $I'_{W2F}$ 
2: Compute text embedding  $E_T$  from  $t$ 
3: Compute CLIP similarity scores using Eq. (5) and Eq. (6):
4:    $s_{H2F} = \max(100 * \cos(E_{I'_{H2F}}, E_T), 0)$ 
5:    $s_{W2F} = \max(100 * \cos(E_{I'_{W2F}}, E_T), 0)$ 
6: if  $s_{H2F} \geq s_{W2F}$  then
7:    $b^* \leftarrow b^{H2F}$ 
8: else
9:    $b^* \leftarrow b^{W2F}$ 
10: end if
11: return  $b^*$ 

```

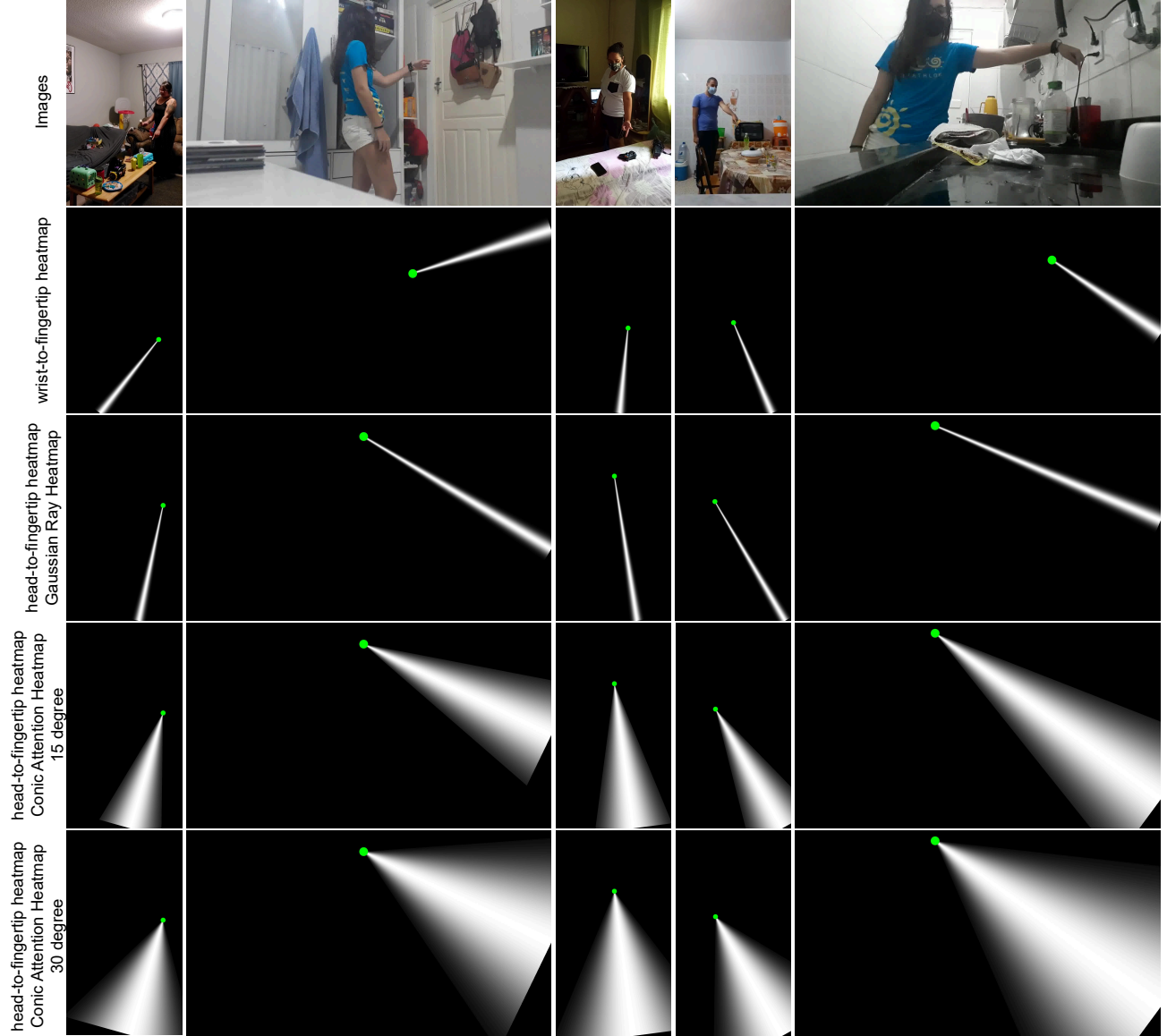


Figure B.4. This figure presents various heatmaps. The first row shows the input images. The second row displays wrist-to-fingertip heatmaps used for training M_{W2F} , while the third row contains head-to-fingertip heatmaps used for training M_{H2F} . The fourth and fifth rows show Conic Attention Heatmaps with 15° and 30° angles, respectively, which are used in the ablation study which we present in Tab. 7.

C.3. CLIP-Only (Top-2 + Threshold)

This method is similar to CLIP-Only (Top-1), where we take predictions from both models and compute the CLIP similarity score between the cropped bounding boxes and the input text. However, unlike the Top-1 variant, we also consider the Top-2 predictions from each model. However, we do not always include the second predictions; instead, we apply a confidence threshold determined empirically on the validation set, $T = 0.95$. If a model’s second-highest

prediction has a confidence score greater than or equal to this threshold, it is included in the comparison. Finally, we select the bounding box with the highest CLIP similarity score as the final prediction. The algorithm for this method is presented in Algorithm C.3.

C.4. CLIP Fusion

In this method, we leverage both the CLIP similarity score and the model’s confidence score to make the final prediction. Specifically, we compute a hybrid score for each

Algorithm C.3 Algorithm for CLIP-Only (Top-2 + Threshold).

Require: Predictions from models M_{H2F} and M_{W2F} , confidence threshold $T = 0.95$, input text t

Ensure: Final bounding box prediction b^*

```

1: Extract top-2 predictions from each model:
2:    $P_{H2F} = \{(b_1^{H2F}, c_1^{H2F}), (b_2^{H2F}, c_2^{H2F})\}$ 
3:    $P_{W2F} = \{(b_1^{W2F}, c_1^{W2F}), (b_2^{W2F}, c_2^{W2F})\}$ 
4: Initialize candidate set  $\mathcal{B} = \{b_1^{H2F}, b_1^{W2F}\}$ 
5: if  $c_2^{H2F} \geq T$  then
6:   Add  $b_2^{H2F}$  to  $\mathcal{B}$ 
7: end if
8: if  $c_2^{W2F} \geq T$  then
9:   Add  $b_2^{W2F}$  to  $\mathcal{B}$ 
10: end if
11: for each  $b \in \mathcal{B}$  do
12:   Compute CLIP similarity score  $s_b = \text{CLIP}(b, t)$ 
13: end for
14:  $b^* = \arg \max_{b \in \mathcal{B}} s_b$ 
15: return  $b^*$ 

```

bounding box by summing its confidence score and its CLIP similarity score. We use the Top-2 predictions from both models for this process. However, the CLIP similarity scores and model confidence scores operate on different scales: while confidence scores are normalized in the range $[0, 1]$, CLIP similarity scores typically range around 25. To balance their influence and prevent the CLIP score from dominating, we scale the CLIP similarity scores by a factor of 0.04. The scaled CLIP score is then added to the corresponding confidence score to compute the final hybrid score for each bounding box. Finally, we select the bounding box with the highest hybrid score as the final prediction. The algorithm for this method is presented in Algorithm C.4.

C.5. CLIP-Aware Pointing Ensemble (CAPE)

In this method, we combine the CLIP-Only (Top-2 + Threshold) and CLIP Fusion approaches. Through empirical analysis on validation set, we observe that for small objects, the CLIP Fusion method yields more accurate results than other ensemble strategies. This is primarily because CLIP tends to perform less reliably on smaller objects. Therefore, we apply CLIP Fusion to not rely on only CLIP-score but also consider the confidence score. To determine whether an object is small, we follow the definition provided by [11]: if the object occupies less than 0.48% of the total image area, we classify it as small and use the CLIP Fusion ensemble. For all other cases, we apply the CLIP-Only (Top-2 + Threshold) method. The algorithm is presented in Algorithm C.5.

Algorithm C.5 CLIP-Aware Pointing Ensemble (CAPE) algorithm.

Require: Top-2 predictions from models M_{H2F} and M_{W2F} , input text t , object area threshold $\tau = 0.0048$

Ensure: Final bounding box prediction b^*

```

1: Extract candidate bounding boxes from both models
2: Estimate area ratio  $r$  of each candidate bounding box to the image size
3: if  $r < \tau$  then
4:    $b^* = \text{ConfidenceCLIPFusion}(M_{H2F}, M_{W2F}, t)$  // Refer to Algorithm C.4
5: else
6:    $b^* = \text{CLIPOnlyTop2Threshold}(M_{H2F}, M_{W2F}, t)$  // Refer to Algorithm C.3
7: end if
8: return  $b^*$ 

```

Name	Value
Learning rate vision backbone	$1e-5$
Learning rate - text backbone	$1e-4$
Learning rate	$1e-5$
λ_1	2
λ_2	1
λ_3	10
λ_4	10
λ_5	1
λ_6	1
Transformer encoder layer	6
Transformer decoder layer	6
Number of attention heads per layer	8
MLP dimension	2048
Dropout	$p = 0.1$
Weight decay	$1e-4$
Batch size	4
Text encoder	Roberta-Base
Image encoder	ResNet-101
Heatmap encoder	ResNet-18
Position embedding	Sine
Input dim of transformer encoder	256
Number of queries	20

Table C.8. Hyperparameters and other training details.

D. Finetuning or Frozen Text Encoder?

Based on multiple training experiments, we observed that finetuning the text encoder sometimes leads to instability, represented by the pink line in Fig. E.5. In contrast, freezing the text encoder results in consistently stable training, as shown by the green and orange lines in Fig. E.5. Therefore, achieving stable training with a finetuned text encoder

Algorithm C.4 Algorithm of CLIP Fusion method.

Require: Top-2 predictions from models M_{H2F} and M_{W2F} , input text t , scaling factor $\lambda = 0.04$

Ensure: Final bounding box prediction b^*

```
1: Extract top-2 predictions:
2:    $P_{H2F} = \{(b_1^{H2F}, c_1^{H2F}), (b_2^{H2F}, c_2^{H2F})\}$ 
3:    $P_{W2F} = \{(b_1^{W2F}, c_1^{W2F}), (b_2^{W2F}, c_2^{W2F})\}$ 
4: Initialize candidate set  $\mathcal{B} = \{(b_1^{H2F}, c_1^{H2F}), (b_2^{H2F}, c_2^{H2F}), (b_1^{W2F}, c_1^{W2F}), (b_2^{W2F}, c_2^{W2F})\}$ 
5: for each  $(b, c) \in \mathcal{B}$  do
6:   Compute CLIP similarity score  $s = \text{CLIP}(b, t)$ 
7:   Compute hybrid score  $h = c + \lambda \cdot s$ 
8:   Store  $(b, h)$ 
9: end for
10:  $b^* = \arg \max_{(b, h)} h$ 
11: return  $b^*$ 
```

requires several attempts. However, despite this challenge, finetuning the text encoder ultimately yields better performance.

E. Hyperparameters and Other Training Parameters

In Tab. C.8, we present empirically determined hyperparameters and other key training details to support reproducibility.

F. More Results

In Tab. F.9, we report the mAP at three different thresholds for all ablation setups, categorized by object size. Similarly, in Tab. F.10, we present the CLIP scores and C_D metrics for the same setups, also with respect to object size.

In Fig. F.6, we present examples of failure cases. In the first row, although our model M_{H2F} correctly detects the target object, CAPE selects the prediction from M_{W2F} , which is incorrect in this case. In the second row, the bottles are extremely difficult to distinguish, even with explicit pointing cues. Nevertheless, the predicted bounding boxes cover other bottles adjacent to the GT one, which is acceptable, as they overlap with the pointing line and are semantically consistent with the text. In the third row, both of our models, as well as the Touch-Line models, produce incorrect predictions. However, guided by the pointing information, the predictions from M_{H2F} and M_{W2F} lie on the pointing line and are very close to the GT object. In contrast, the Touch-Line predictions are entirely off the pointing line and significantly distant from the GT object.

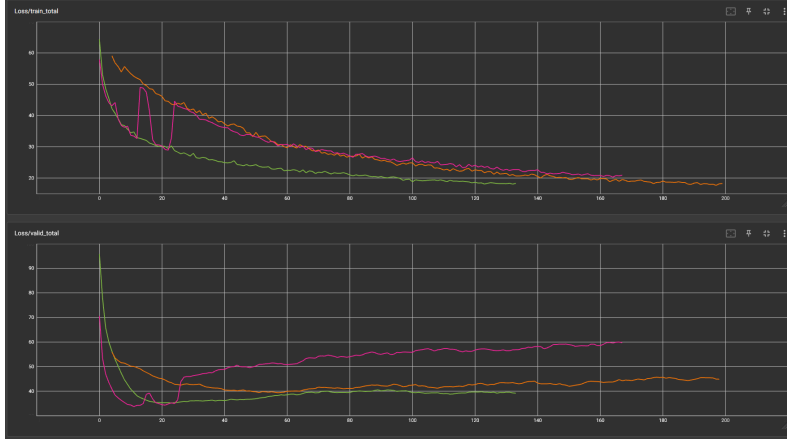


Figure E.5. Graphs of training and validation loss from three separate runs are shown. The green and pink lines represent training with a finetuned text encoder, while the orange line corresponds to training with a frozen text encoder.

IoU Threshold for mAP				0.25				0.50				0.75			
Setup	Object Sizes	Heatmap Injection	Ensemble	All	S	M	L	All	S	M	L	All	S	M	L
	Touch-Line-EWL [35]	-	-	69.5	56.6	71.7	80.0	60.7	44.4	66.2	71.2	35.5	11.8	38.9	55.0
	Touch-Line-VTL [35]	-	-	71.1	55.9	75.5	81.7	63.5	47.0	70.2	73.1	39.0	13.4	45.2	57.8
1	Baseline	-	-	71.2	59.8	73.0	80.9	60.1	43.2	66.4	70.5	32.8	8.6	35.4	53.4
2	Setup 1 + object center prediction	-	-	70.8	59.5	73.2	79.5	61.7	45.8	67.4	71.5	34.6	14.0	38.1	51.1
3	Setup 1 + W2F heatmap	Embedding feature	-	68.9	55.5	74.0	77.4	59.7	42.0	68.1	69.3	32.4	8.7	37.8	50.6
4	Setup 1 + H2F heatmap	Embedding feature	-	71.9	57.5	74.1	84.1	62.8	43.3	70.1	75.1	33.8	10.0	35.6	55.3
5	Setup 2 + W2F heatmap	Embedding feature	-	69.6	57.7	74.9	76.4	60.7	45.5	69.0	68.2	31.5	12.1	35.3	47.0
6	Setup 2 + H2F heatmap	Embedding feature	-	72.9	59.5	77.8	81.4	62.3	44.3	70.9	42.0	35.1	10.4	39.3	55.3
7	Setup 1 + W2F heatmap + H2F heatmap	Embedding feature	-	70.2	59.0	71.4	80.2	60.2	44.5	65.6	70.5	33.8	11.9	39.3	50.0
8	Setup 6	Channel-wise input	-	68.7	58.5	71.9	75.6	58.5	44.8	65.0	65.9	33.4	13.9	37.4	48.6
9	Setup 6	Channel-wise feature	-	72.6	60.0	77.5	80.4	58.4	38.8	68.7	68.1	27.9	8.5	32.6	42.5
10	Setup 5 + Setup 6	Embedding feature	Confidence-Only	73.4	62.7	78.6	79.0	64.1	49.0	72.7	71.0	34.1	13.4	38.2	50.5
11	Setup 5 + Setup 6	Embedding feature	CLIP-Only (Top-1)	73.5	59.7	79.9	81.2	64.2	46.5	74.3	72.2	35.4	12.7	39.8	53.4
12	Setup 5 + Setup 6	Embedding feature	CLIP-Only (Top-2 + Threshold)	73.8	59.7	80.2	81.6	64.1	46.3	74.3	72.2	35.5	12.4	40.1	53.9
13	Setup 5 + Setup 6	Embedding feature	CLIP Fusion	73.6	63.2	78.4	79.6	64.4	49.3	72.8	71.7	34.5	13.4	38.5	51.7
14	Setup 5 + Setup 6	Embedding feature	CAPE	75.0	63.2	80.2	81.8	65.4	49.5	74.3	72.7	35.7	13.4	40.1	53.4
15	Setup 6 w/ frozen text encoder	Embedding feature	-	71.3	56.0	74.9	83.1	62.1	42.5	69.5	74.4	33.7	10.2	35.8	54.6
16	Setup 6 w/ Conic Attention Heatmap (15°)	Embedding feature	-	70.0	54.2	72.2	83.3	60.0	42.0	66.6	71.5	33.9	12.2	40.6	48.8
17	Setup 6 w/ Conic Attention Heatmap (30°)	Embedding feature	-	71.5	58.7	73.5	82.1	59.4	41.8	64.7	71.7	30.8	7.0	32.4	52.7
Ours - Final				75.0	63.2	80.2	81.8	65.4	49.5	74.3	72.7	<u>35.7</u>	13.4	<u>40.1</u>	<u>53.4</u>

Table F.9. Detailed mAP results of all ablation setups with respect to the object size.

				CLIP Score				C_D			
Setup	Object Sizes	Heatmap Injection	Ensemble	All	S	M	L	All	S	M	L
	Touch-Line-EWL [35]	-	-	0.7369	0.6936	0.7305	0.7845	0.3168	0.3006	0.2903	0.3564
	Touch-Line-VTL [35]	-	-	0.7368	0.6925	0.7321	0.7846	0.2843	0.2809	0.2276	0.3393
1	Baseline	-	-	0.7409	0.7003	0.7341	0.7861	0.2662	0.2182	0.2506	0.3266
2	Setup 1 + object center prediction	-	-	0.7339	0.6947	0.7277	0.7787	0.2707	0.2201	0.2692	0.3222
3	Setup 1 + W2F heatmap	Embedding feature	-	0.7353	0.6934	0.7297	0.7812	0.2984	0.2763	0.2616	0.3533
4	Setup 1 + H2F heatmap	Embedding feature	-	0.7375	0.6936	0.7333	0.7852	0.2694	0.2649	0.2233	0.3172
5	Setup 2 + W2F heatmap	Embedding feature	-	0.7344	0.6939	0.7306	0.7780	0.2770	0.2568	0.2319	0.3382
6	Setup 2 + H2F heatmap	Embedding feature	-	0.7373	0.6953	0.7343	0.7819	0.249	0.222	0.2202	0.3024
7	Setup 1 + W2F heatmap + H2F heatmap	Embedding feature	-	0.7345	0.6965	0.7277	0.7780	0.2744	0.2540	0.2314	0.3335
8	Setup 6	Channel-wise input	-	0.7348	0.6933	0.7273	0.7828	0.2959	0.2437	0.2642	0.3767
9	Setup 6	Channel-wise feature	-	0.7372	0.6953	0.7311	0.7839	0.2598	0.2289	0.2119	0.3339
10	Setup 5 + Setup 6	Embedding feature	Confidence-Only	0.7735	0.7441	0.7843	0.7923	0.247	0.2176	0.2042	0.3141
11	Setup 5 + Setup 6	Embedding feature	CLIP-Only (Top-1)	0.7932	0.7688	0.8010	0.8098	0.2391	0.2242	0.2011	0.2878
12	Setup 5 + Setup 6	Embedding feature	CLIP-Only (Top-2 + Threshold)	0.7379	0.7967	0.7343	0.7819	0.2422	0.2158	0.2009	0.3060
13	Setup 5 + Setup 6	Embedding feature	CLIP Fusion	0.7742	0.7927	0.7455	0.7842	0.2434	0.2137	0.2028	0.3090
14	Setup 5 + Setup 6 (Final Model)	Embedding feature	CAPE	0.7983	0.7927	0.8015	0.8010	0.2476	0.2137	0.2241	0.3023
15	Setup 6 w/ frozen text encoder	Embedding feature	-	0.7382	0.6954	0.7323	0.7855	0.2634	0.2626	0.2233	0.3006
16	Setup 6 w/ Conic Attention Heatmap (15°)	Embedding feature	-	0.7387	0.6962	0.7325	0.7860	0.2695	0.2685	0.2344	0.3028
17	Setup 6 w/ Conic Attention Heatmap (30°)	Embedding feature	-	0.7391	0.6970	0.7332	0.7863	0.2765	0.2750	0.2499	0.3026
Ours - Final				0.7983	0.7927	0.8015	0.8010	0.2476	0.2137	0.2241	0.3023

Table F.10. Detailed CLIP scores and C_D metrics of all ablation setups with respect to the object size.



Figure F.6. Some examples for failure cases.